



ELSEVIER

Nuclear Instruments and Methods in Physics Research A 482 (2002) 653–666

**NUCLEAR  
INSTRUMENTS  
& METHODS  
IN PHYSICS  
RESEARCH**  
Section A

www.elsevier.com/locate/nima

# A new numerical technique to design satellite energetic electron detectors

M.G. Tuszewski\*, T.E. Cayton, J.C. Ingraham

*Los Alamos National Laboratory, Group NIS-2, MS D436, Los Alamos, NM 87545, USA*

Received 18 May 2001; accepted 23 July 2001

## Abstract

Energetic charged particles trapped in the magnetosphere are routinely detected by satellite instruments. However, it is generally difficult to extract quantitative energy and angular information from such measurements because the interaction of energetic electrons with matter is rather complex. Beam calibrations and Monte-Carlo (MC) simulations are often used to evaluate a flight instrument once it is built. However, rules of thumb and past experience are common tools to design the instrument in the first place. Hence, we have developed a simple numerical procedure, based on analytical probabilities, suitable for instrumental design and evaluation. In addition to the geometrical response, the contributions of surface backscattering, edge penetration, and bremsstrahlung radiation are estimated. The new results are benchmarked against MC calculations for a simple test case. Complicated effects, such as the contribution of the satellite to the instrumental response, can be estimated with the new formalism. © 2002 Elsevier Science B.V. All rights reserved.

*PACS:* 95.55; 94.80

*Keywords:* Numerical technique; Electron detector

## 1. Introduction

The energetic (10 keV–10 MeV) charged particle populations trapped in the earth's magnetosphere are routinely sampled by satellite instruments. Quantitative measurements are important because penetrating charged particles can cause severe damage to satellite electronics. Quantitative measurements are also necessary for magnetospheric science, when charged particle data from different

satellites must be compared. However, it is difficult to extract quantitative energy and angular information from energetic electron measurements because material penetration, surface backscattering, and bremsstrahlung radiation can greatly complicate the instrumental response [1]. While the detection of energetic ions is generally more straightforward, contamination of ion channels by energetic electrons also occurs frequently.

Electron beam calibrations and Monte-Carlo (MC) simulations are frequently used to assess the performance of a flight instrument once it is built. However, these complex and costly tools are not often used for instrumental design. Instead, rules

\*Corresponding author. Tel.: +1-505-667-3566; fax: +1-505-665-4414.

E-mail address: mgtu@lanl.gov (M.G. Tuszewski).

of thumb and past experience mainly prevail. The instrumental response is often assumed to reflect the geometry of collimators or apertures. Shielding materials are selected empirically to reduce possible other contributions. It would be highly desirable to use less-computer-intensive calculations than MC simulations to design and evaluate quantitatively an instrument in the first place. Hence, the motivation for the present study.

We present here a numerical procedure based on analytical probabilities suitable to design a solid-state energetic electron detector. This formalism is referred to as AP (acronym for Analytical Probability) in this paper. The AP calculations extend the geometrical response analysis of Sullivan [2] to important other contributions, including backscattering, edge penetration, and bremsstrahlung radiation. These effects are estimated with the AP formalism and are compared to MC calculations for a simple test case.

The AP and MC calculations are described in Section 2. The geometrical response of the test case is considered in Section 3. The effects of angular scattering are discussed and the contribution of surface backscattering is estimated in Section 4. The edge cut trajectories, that can result from material penetration and from angular scattering, are analyzed in Section 5. The often dominant contribution of bremsstrahlung photons is derived in Section 6. Finally, the AP calculation is applied to a real satellite instrument in Section 7, including the substantial satellite contribution to the instrumental response. The results are discussed, and some conclusions are offered in Section 8.

## 2. Analytical probability and MC calculations

The geometrical response of a satellite instrument has been evaluated by Sullivan [2]. The AP formalism generalizes Sullivan's analysis to other electron trajectories that can contribute substantially to the instrumental response. Indeed, scattered or penetrating electrons, and secondary bremsstrahlung photons can often be detected in larger numbers than electrons passing through geometrical apertures. The AP calculations consider the most important types of electron

trajectories from the top surface of the instrument down to the detector. For each electron trajectory,  $k$ , an overall detection efficiency,  $\varepsilon_k$ , is defined analytically by multiplying the probabilities of each step of the trajectory. In general,  $\varepsilon_k$  depends on the incident electron energy,  $E$ , on the incident unit vector direction,  $u$ , on the electron impact point,  $P$ , and on the top surface of the instrument. Spherical angles  $(\theta, \phi)$  around an axis,  $n$ , normal to the top surface at point  $P$ , are used to characterize  $u$ .

An incident differential electron flux  $j$  ( $\text{mm}^{-2} \text{sr}^{-1} \text{MeV}^{-1} \text{s}^{-1}$ ), spatially uniform and time independent, is assumed on the top surface of the instrument. The energy and angular dependences of  $j$  are assumed separable, so that one can write  $j = j_0(E)F(\theta, \phi)$ . The directional response,  $A_k$  ( $\text{mm}^2$ ), of the instrument can then be expressed as

$$A_k(E, \theta, \phi) = \int \varepsilon_k(E, \theta, \phi, P) F(\theta, \phi) u \, d\sigma \quad (1)$$

where  $d\sigma$  is a top surface element around  $P$ , and the integral includes all top surface area where  $\varepsilon_k$  is finite. One has  $u \, d\sigma = (un) \, d\sigma = \cos(\theta) \, d\sigma$  in Eq. (1). The instrument gathering power,  $\Gamma_k$  ( $\text{mm}^2 \text{sr}$ ), corresponding to the electron trajectory  $k$ , is obtained by integrating  $A_k$  over the entire incident solid angle. One can write

$$\Gamma_k(E) = \int d\phi \int A_k(E, \theta, \phi) \sin(\theta) \, d\theta \quad (2)$$

where the integrals are performed over  $0 < \phi < 2\pi$  and  $0 < \theta < \pi/2$ , respectively. The associated instrument counting rate,  $C_k$  ( $\text{s}^{-1}$ ), is then obtained as

$$C_k = \int j_0(E) \Gamma_k(E) \, dE. \quad (3)$$

A cylindrical collimator, sketched in Fig. 1, is used as a simple example relevant to satellite instruments. A monoenergetic disk electron source (radius  $r_s = 2.5 \text{ mm}$ ) is placed  $1 \mu\text{m}$  above the cylindrical collimator (radius  $r_p = 0.5 \text{ mm}$  and length  $L = 6 \text{ mm}$ ). A large cylindrical detector (radius  $r_d = 10 \text{ mm}$  and thickness  $L_d = 5 \text{ mm}$ ) is located  $0.5 \text{ mm}$  below the collimator. The source, collimator, and detector have azimuthal ( $\phi$ )

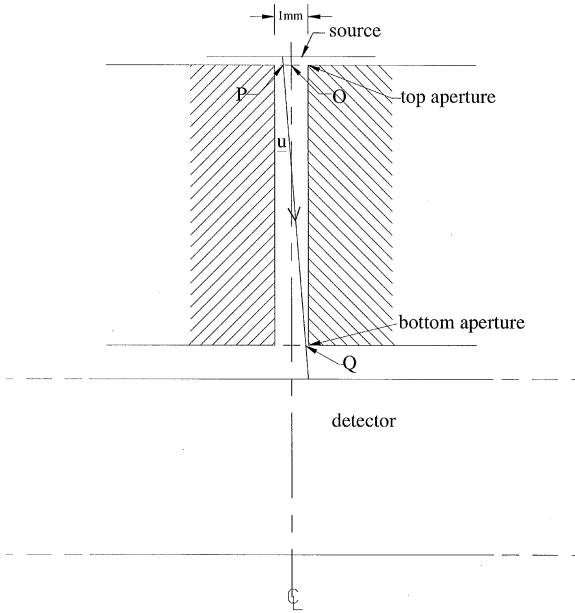


Fig. 1. Sketch of the test case, including disk electron source, collimator, and detector.

symmetry around the vertical  $z$ -axis issued from the middle (point  $O$ ) of the top aperture.

Electrons are emitted from the bottom surface of the disk source with equal intensity in all directions. This approximates a thin internal electron conversion line from a radioactive calibration source [3]. The electron flux incident on the top surface is not isotropic ( $F = 1$ ) because more electrons come from the edge of the disk source than from the center. One derives  $F = 1/\cos(\theta)$  for the above disk source, so that the product  $Fu d\sigma$  in Eq. (1) reduces to  $d\sigma$ . Any impact point  $P$  on the top surface can be located with a radius  $\rho_p$  and an angle  $\phi_p$ . Azimuthal symmetry in Fig. 1 permits one to write  $d\sigma = 2\pi\rho_p d\rho_p$ , and Eq. (1) reduces to a single integral over the radius  $\rho_p$ .

The supporting MC calculations in this paper are made with the MCNP transport code [4]. MCNP follows the primary electrons and all their issues, including photons. This code, developed and refined over many years, allows for complicated geometrical objects and multiple materials. Any surface can be chosen to be “ideal”, that is,

fully absorbing for all species that intersect it. This option will be often used in the following Sections to study specific electron trajectories. A typical MCNP calculation considers a large number ( $N = 12.8$  or  $51.2$  million) of electrons of energy  $E$ , emitted in all downward directions ( $2\pi$  solid angle) from the disk source.

The output of an MC simulation consists of a distribution of counts as a function of energy deposited within the detector volume. The deposited energy includes all species issued from a particular source electron. The counts are distributed in 10-keV-wide energy bins, and the total counts are obtained by summing all energy bins. In the MC calculation, the instrument gathering power can be inferred from the total count rate. One can write  $j_0(E) = N\delta(E)/(2\pi A_s)$  for the disk source, where  $\delta$  is the delta function, and where  $A_s = \pi r_s^2$  is the source area. Then, one obtains from Eq. (3)

$$\Gamma_k = (2\pi A_s/N)C_k. \quad (4)$$

The above gathering power from the MC calculation can be compared to that obtained with Eq. (2) of the AP formalism for a specific class  $k$  of electron trajectory. Of course, the comparison is meaningful only if the MC counts are largely dominated by electrons with trajectory  $k$ .

### 3. Geometry

The geometrical response of the collimator sketched in Fig. 1 is first calculated. This is the ideal response that comes from all straight electron trajectories that do not intercept the top, side, or bottom surfaces of the collimator. Only points  $P$  within the top aperture area contribute to the geometrical response. An example of geometrical electron trajectory ( $k = g$ ) is sketched in Fig. 2(a). For the collimator of interest, the geometrical efficiency can be simply defined as

$$\varepsilon_g = H(r_p - \rho_q) \quad (5)$$

where  $H$  is the Heaviside function ( $H(x) = 1$  if  $x > 0$ ,  $H = 0$  otherwise), and  $\rho_q$  is the radius of the point  $Q$  where the electron intersects the bottom aperture. For a given incident vector  $u(\theta, \phi)$  at a

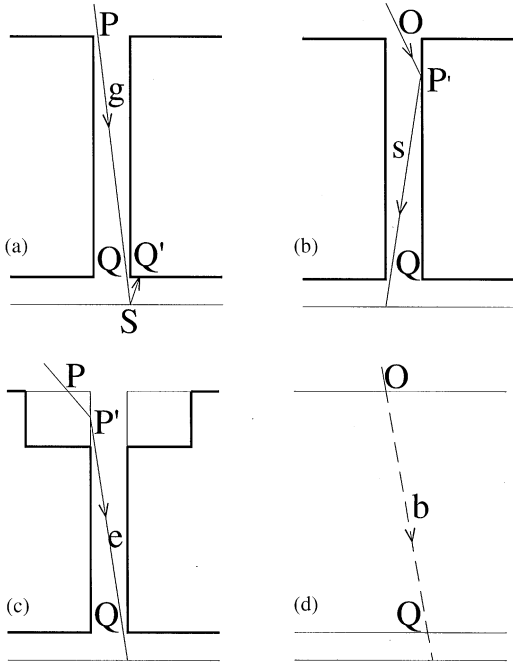


Fig. 2. The main classes of electron trajectories, yielding (a) geometrical, (b) wall backscattering, (c) edge cut, and (d) bremsstrahlung instrumental responses. The ideal surfaces used in the Monte-Carlo calculations are indicated with heavy lines.

point  $P(\rho_p)$  of the top surface, one has

$$\rho_q(\rho_p, \theta, \phi) = [\rho_p^2 + L^2 \tan^2(\theta) + 2L\rho_p \tan(\theta) \cos(\phi)]^{1/2}. \quad (6)$$

The geometrical directional response  $A_g(\theta, \phi)$  is calculated from Eq. (1), with  $0 < \rho_p < r_p$ , and with  $\varepsilon_g(\rho_p, \phi, \theta)$  derived from Eqs. (5) and (6). A geometrical gathering power  $\Gamma_g = 0.0171 \text{ mm}^2 \text{ sr}$  is then computed from Eq. (2).

For elongated collimators ( $r_p/L \ll 1$ ) such as in Fig. 1, the AP calculations can be much simplified without appreciable loss of accuracy by assuming that  $P \rightarrow O$  ( $\rho_p \rightarrow 0$ ). With this approximation, one obtains  $\rho_q = L \tan(\theta)$ ,  $\varepsilon_g = H(\theta_1 - \theta)$ , and  $A_g = A_p H(\theta_1 - \theta)$  from Eqs. (6), (5) and (1), respectively. In these expressions,  $\tan(\theta_1) = r_p/L$  and  $A_p = \pi r_p^2$ . Finally, Eq. (2) yields  $\Gamma_g = 2\pi A_p [1 - \cos(\theta_1)] = 0.0170 \text{ mm}^2 \text{ sr}$ , a result essentially identical to that obtained without approximation. One has  $\Gamma_g \sim (A_p/L)^2$ , which is the expected [2]

product of the aperture area  $A_p$  by the collimator solid angle  $\Omega \sim A_p/L^2$ . Inserting  $\Gamma_g \sim (A_p/L)^2$  into Eq. (3) or (4), one obtains  $C_g \sim (NA_p/A_s)(\Omega/2\pi)$ . This expression implies that  $C_g$  is the number of electrons entering the top aperture multiplied by the fraction of those electrons passing through the bottom aperture.

An MC calculation of the geometrical response of the collimator in Fig. 1 is made by choosing ideal (perfectly absorbing) top, side, and bottom collimator surfaces. All ideal surfaces in the MC calculations are indicated with heavy solid lines in Fig. 2.  $N = 12.8$  million electron trajectories are issued from the disk source. A relatively low electron energy,  $E = 0.25 \text{ MeV}$ , is selected to insure that no electron can penetrate the detector thickness. Several calculations, with various detector materials, yield total counts of  $1772 \pm 4$ . The 4 counts uncertainty is statistical, as evidenced by repeated calculations with identical initial conditions. The total counts reflect  $C_g$  since non-geometrical electron trajectories are terminated by the ideal surfaces. Using  $C_g = 1772$  in Eq. (4) yields  $\Gamma_g = 0.0171 \text{ mm}^2 \text{ sr}$ , the same value as obtained with the AP formalism.

#### 4. Backscattering

Electrons are deflected from their initial direction as they penetrate materials because of elastic scattering by atomic nuclei and their electrons [5]. The electrons that pass through thin materials acquire Gaussian angular distributions around their incident trajectories [6]. For thicker materials, the Gaussian profiles evolve in cosine-like angular distributions [5,7].

As a result of angular scattering, some of the electrons incident on a given surface can backscatter with a fraction of their initial energy [5,7,8]. An example of backscattering, off a detector surface, is sketched in Fig. 2(a) with the segment  $SQ'$ . Detector backscattering always occurs to some degree, and complicates the count distributions of MC calculations of the geometrical response. Examples are shown in Fig. 3 for beryllium, silicon, and tungsten detectors. While most of the counts are found in the full energy bin,

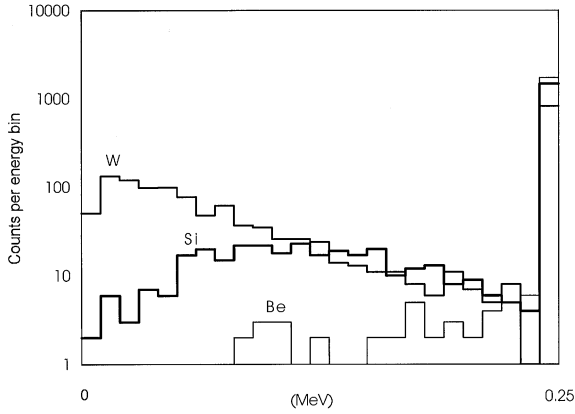


Fig. 3. Monte-Carlo count distributions as functions of the energy deposited into the detector volume. The distributions result from the geometrical test case of Fig. 2(a), assuming tungsten, silicon, and beryllium detectors.

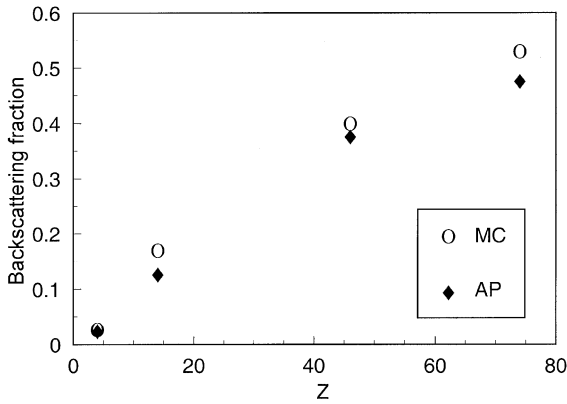


Fig. 4. Calculated backscattering coefficients for normal incidence on materials, as function of the material atomic number. The results of Monte-Carlo and AP calculations are indicated with open circles and solid diamonds, respectively.

as expected for electron trajectories through apertures, the counts in the lower energy bins are caused by detector backscattering.

Backscattering coefficients are defined as ratios of reflected to incident electrons. Normal incidence backscattering coefficients can be inferred from the count distributions of Fig. 3, as the ratios of the counts found in energy bins are less than 0.25 MeV to the total counts. Such ratios are shown with open circles in Fig. 4 for different material  $Z$  values. The ratios agree well with the analytical

backscattering coefficients  $\eta$  of Tabata [8] that are shown with solid diamonds in Fig. 4. We adopt Tabata's coefficients as our AP backscattering probabilities.

Backscattering increases with the material  $Z$  value, as can be seen in Fig. 4. For example, about 40% of the electrons that impact a CdZnTe detector with normal incidence are backscattered. In addition, the average energy of the backscattered electrons increases for higher  $Z$  materials [7]. This effect can be observed in the MC spectra of Fig. 3, where more counts are found in lower energy bins for higher  $Z$  materials. Backscattering is essentially independent of electron energy for  $E < 1$  MeV and decreases for higher  $E$  values [8].

Backscattering increases as the angle of incidence,  $\psi = \pi/2 - \theta$ , decreases [7]. Grazing incidence ( $\psi \rightarrow 0$ ) on any material leads to backscattering coefficients approaching unity. Grazing incidence backscattering occurs essentially as specular reflection, with projected backscattered angles  $\Phi \sim \psi$ . Finally, grazing incidence backscattering results in little electron energy loss. We have extracted, from the detailed experimental results of Von Frank [7], some approximate analytical functions for the differential backscattering probabilities  $dp/d\Omega(\psi, \Phi, Z, E)$ . These functions are chosen so that the backscattering coefficients  $p = \int (dp/d\Omega) d\Omega$  satisfy the limits:  $p \rightarrow 1$  as  $\psi \rightarrow 0$  and  $p \rightarrow \eta$  as  $\psi \rightarrow \pi/2$ .

Collimator wall backscattering is an important process for satellite instruments. An example of this class ( $k = s$ ) of electron trajectory is sketched in Fig. 2(b). An electron that enters the top aperture at  $P$  is backscattered from a point  $P'$  of the side wall into the bottom aperture. For a given incident electron direction, the detection efficiency,  $\varepsilon_s$ , is defined as

$$\varepsilon_s = \int (dp/d\Omega) d\Omega \quad (7)$$

where the integral is performed over the solid angle of the bottom aperture viewed from  $P'$ . We have also estimated and added to Eq. (7) the contribution of electron trajectories that make two bounces off the side wall. The resulting efficiencies  $\varepsilon_s$  are then inserted in Eq. (1), which reduces to  $A_s(E, \theta) = A_p \varepsilon_s(E, \theta)$  with

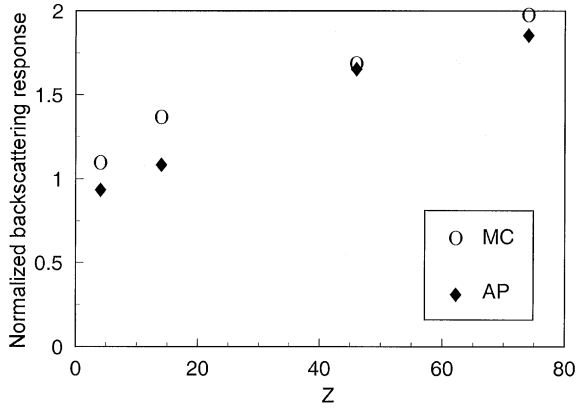


Fig. 5. Collimator wall backscattering response, normalized to the geometrical response, for various slab materials. The normalized responses are calculated for the test case of Fig. 2(b) as functions of the slab material atomic number.

the  $P \rightarrow O$  approximation. This approximation, detailed in Section 3, proves again to be accurate and numerically simple for the elongated collimator of Fig. 1. Then,  $\Gamma_s(E)$  is obtained from Eq. (2).

The ratios  $\Gamma_s/\Gamma_g$ , calculated with the AP formalism for  $E = 0.1$  MeV, are shown with solid diamonds in Fig. 5 for several collimator materials. The corresponding ratios inferred from MC calculations are also shown in Fig. 5 with open circles. The MC calculations use  $N = 12.8$  million electrons and assume ideal top and bottom surfaces. The low  $E$  value (0.1 MeV) insures a negligible bremsstrahlung contribution. The MC total counts include mostly geometrical and wall scattering contributions. The wall scattering counts,  $C_s$ , are estimated by subtracting  $C_g = 1772$  from the total counts. Then,  $\Gamma_s/\Gamma_g = C_s/C_g$  is used to obtain the MC points of Fig. 5.

The AP and MC calculations agree within about 20%. The wall scattering response is comparable or greater than the geometrical response for all materials. The scattering contribution increases approximately as  $Z^{1/4}$  for the collimator of Fig. 1. This scaling is similar, but weaker, than that of normal incidence backscattering in Fig. 4. A collimator aspect ratio scaling,  $\Gamma_s/\Gamma_g \sim (r_p/L)^{1/2}$ , is derived from other AP calculations where  $r_p$  and  $L$  are varied.

## 5. Edge cut

Energetic electrons can penetrate through material thicknesses comparable to their practical range  $R$  [9]. The actual electron path lengths are generally larger than  $R$  because of angular scattering. Electron penetration through collimator corners results in a class ( $k = e$ ) of electron trajectories sketched in Fig. 2(c), that can be an important contribution to the instrumental response. Only electrons incident on the top surface within a distance of a few  $R$  from the aperture contribute to the edge cut response. An electron incident at  $P$  reenters the collimator side wall at  $P'$ , and passes through the bottom aperture at  $Q$ . The electron can change direction from  $PP'$  to  $P'Q$  because of angular scattering. The edge cut trajectories confuse the energy resolution of the instrument because edge cut electrons can deposit any energy up to  $E$  into the sensor, depending on the path length  $PP'$ .

The transmission probability,  $T$ , for a given distance  $PP'$  through a material, is defined as the ratio of transmitted to incident electrons. Transmission data through aluminum foils [10] suggests that  $T$  can be approximated in terms of a dimensionless variable  $x = PP'/R$  as

$$T(x) = \begin{cases} 1 - 2x^3, & 0 < x \leq 0.5 \\ 1.5(1 - x), & 0.5 < x \leq 0.9 \\ 0.15 \exp(-10x + 9), & 0.9 < x. \end{cases} \quad (8)$$

The detection efficiency  $\varepsilon_e$ , associated with an edge cut trajectory  $e$ , can then be defined in terms of  $T$  as

$$\varepsilon_e = (1 - p)T(x)f_e \quad (9)$$

where  $p$  is the backscattering probability at point  $P$ , and  $f_e$  is the fraction of the electrons that are redirected from  $P'$  within the bottom aperture. The fraction  $f_e$  is evaluated assuming that the electron distribution at  $P'$  is proportional to the cosine of the polar angle around the incident direction  $PP'$ . The directional response  $A_e(E, \theta, \phi)$  and the gathering power  $\Gamma_e(E)$  are obtained by performing numerically the integrals of Eqs. (1) and (2), respectively, with  $\varepsilon_e(E, \theta, \phi, \rho_p)$  taken from Eq. (9).

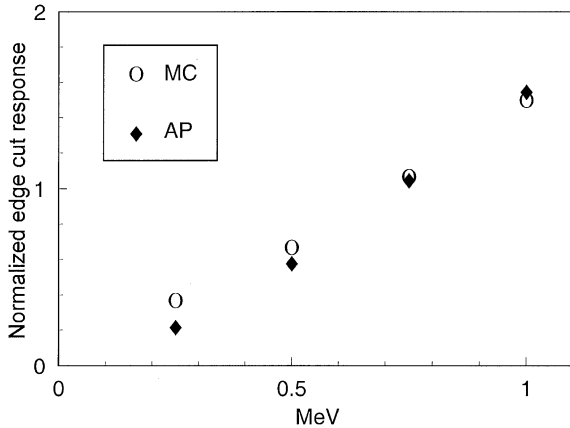


Fig. 6. Edge cut response, normalized to the geometrical response, for various incident electron energies. The normalized responses are calculated for the test case of Fig. 2(c) with beryllium slab material.

The ratios  $\Gamma_e/\Gamma_g$  are computed for the collimator geometry of Fig. 1 and for various electron energies  $E$  up to 1 MeV. The collimator material is chosen to be beryllium to enhance the edge cut response, relative to wall scattering and bremsstrahlung contributions, in the MC calculations. The ratios  $\Gamma_e/\Gamma_g$ , calculated with Eq. (2) of the AP formalism, are shown in Fig. 6 with solid diamonds. The edge cut response increases approximately linearly with electron energy for  $E > 0.5$  MeV. For the test example of Fig. 2(c),  $\Gamma_e$  exceeds  $\Gamma_g$  for energies  $E > 0.7$  MeV. An approximate scaling law,  $\Gamma_e/\Gamma_g \sim R/r_p$ , is obtained from other AP calculations. This scaling is expected because  $\Gamma_e$  comes from an annular area  $\sim 2\pi r_p R$  around the top aperture, while  $\Gamma_g$  comes from the aperture area  $A_p$ . For a given value of  $r_p$ ,  $\Gamma_e/\Gamma_g \sim R$ . This scaling explains the energy dependence of  $\Gamma_e/\Gamma_g$  in Fig. 6, since  $R \sim E$  for  $E > 0.5$  MeV [9].

Monte-Carlo calculations have been performed to estimate the edge cut response of the collimator in Fig. 1. An annular cylindrical volume of beryllium (2 mm width, 2 mm depth) surrounded by ideal surfaces is considered, as sketched in Fig. 2(c). The dimensions of the beryllium are a compromise between two conflicting requirements to isolate the edge cut contribution in the MC calculations. Large dimensions prevent the edge

cut trajectories to intersect the surrounding ideal surfaces for  $E$  up to 1 MeV. Small dimensions reduce two unwanted contributions: edge cut trajectories followed by backscattering off the beryllium portion of the collimator wall, and bremsstrahlung photons generated inside the beryllium annular volume. The edge cut counts,  $C_e$ , are estimated by subtracting the geometrical counts  $C_g$  from the total counts.

The ratios  $\Gamma_e/\Gamma_g = C_e/C_g$  estimated from the MC calculations are shown in Fig. 6 with open circles. There is a good agreement between MC and AP calculations in most cases, except for low electron energies where the MC counts are about twice as large. This discrepancy is presumably due to MC counts, which are due to wall backscattering from the top third of the collimator. Such counts may be significant, compared to the edge cut counts, for sufficiently low electron energies.

## 6. Bremsstrahlung

Energetic electrons lose energy by bremsstrahlung radiation when penetrating materials. Although radiative energy losses are generally small compared to collisional losses, most secondary photons can travel large distances through materials. Hence, many photons reach the detector where they can deposit some energy through photoelectric, Compton, and pair-production interactions. As will be shown later in this paper, bremsstrahlung photons often dominate the instrumental response.

We consider again the test geometry of Fig. 1 to estimate the bremsstrahlung contribution. However, we remove the collimator channel, as shown in Fig. 2(d), to eliminate the geometrical, wall scattering, and edge cut responses in the MC calculations. The bremsstrahlung contribution is not changed much by eliminating the collimator because the aperture area  $A_p$  is much smaller than the source area  $A_s$ . The  $P \rightarrow O$  approximation can again be used successfully in the AP calculations because all points  $P$  are located within a source radius  $r_s$  of  $O$  and because  $r_s$  is smaller than both the slab thickness  $L$  and the detector radius  $r_d$ . The

dotted line portion of the trajectory *b* in Fig. 2(d) illustrates a typical photon trajectory.

The bremsstrahlung yield into the detector, per incident electron of energy *E*, is estimated with the AP formalism by adapting Ferdinand's calculation [11]. Although oblique ( $\theta > 0$ ) electron trajectories are considered in the complete calculations, we only describe normal incidence ( $\theta = 0$ ) electron trajectories to simplify the presentation. Bremsstrahlung photons are produced near the top surface, in the electron penetration layer of thickness *R*. At any point *x* within that layer, the electron has an average energy  $E(x) \sim E(1 - x/R)$ , so that photons are locally generated with energy  $k \leq E(x)$ . At position *x* the electron transmission probability is  $T(x/R)/\cos(\alpha_e)$ , where  $\alpha_e \sim 40^\circ$  accounts for the increased path length due to angular scattering [11]. The photon differential energy spectrum  $dY(k)/dk$  that impacts the detector is obtained by integrating over slab elements. One can write

$$dY/dk = f_d \int \exp[-\mu(L - x)] \times [N_a(T/\cos(\alpha_e)) d\sigma/dk] dx \quad (10)$$

where the integral is taken from the top surface,  $x = 0$ , down to a maximum depth  $R(1 - k/E)$ . The latter comes from the upper bound  $E(x) = k$ . The exponential term inside the integral of Eq. (10) accounts for photon attenuation within the remaining material thickness  $L - x$ ,  $N_a$  is the atomic density, and  $d\sigma/dk$  is the differential radiative cross-section given by Evans [9]. The factor  $f_d$ , in front of the integral of Eq. (10), represents the angular fraction of the photons that reach the detector. This fraction,  $f_d = \int g \Omega_d$ , is derived by integrating the photon angular distribution *g* over the solid detector angle  $\Omega_d$  viewed from the origin. The photon distribution *g* is estimated by convoluting the normal distributions of electrons and photons [11]. For normal incidence, one has

$$g(\beta) = [1/(\theta_e^2 + \theta_b^2)] \exp[-\beta^2/(\theta_e^2 + \theta_b^2)] \quad (11)$$

where  $\beta$  is the photon polar angle, and  $\theta_e$  and  $\theta_b$  are the characteristic normal distribution angles for electrons and bremsstrahlung photons, respectively [11]. The angle  $\theta_b$  is averaged over electron energies. Then, with  $d\Omega \sim 2\pi\beta d\beta$ , one

approximately obtains

$$f_d \sim \Omega_d/[\pi(\theta_e^2 + \theta_b^2)] \quad (12)$$

which is Ferdinand's expression for forward photon direction [11]. Taking into account detector absorption, the total bremsstrahlung yield into the detector becomes

$$Y = \int (dY/dk)[1 - \exp(-\mu_d L_d)] dk \quad (13)$$

where the integral includes all photon energies  $0 < k < E$ , and where  $dY/dk$  is given by Eq. (10). The bremsstrahlung detection efficiency  $\varepsilon_b$  per electron can then be written as

$$\varepsilon_b = (1 - p)Y \quad (14)$$

where *p* is the backscattering coefficient for electrons incident on the top surface.

For the test case of Fig. 2(b), and using the  $P \rightarrow O$  approximation, the detection efficiency  $\varepsilon_b$  is function of *E* and of the incident polar angle  $\theta$ . The directional response  $A_b(E, \theta)$  reduces to  $A_s \varepsilon_b(E, \theta)$ . Then, the gathering power  $\Gamma_b(E)$  is obtained from Eq. (2). The ratios  $\Gamma_b/\Gamma_g$ , computed with the above AP formalism for several electron energies and for three different materials, are shown with solid diamonds in Fig. 7. The values of  $\Gamma_b/\Gamma_g$  are quite large (up to 50) in most cases. The ratios  $\Gamma_b/\Gamma_g$  increase nearly linearly

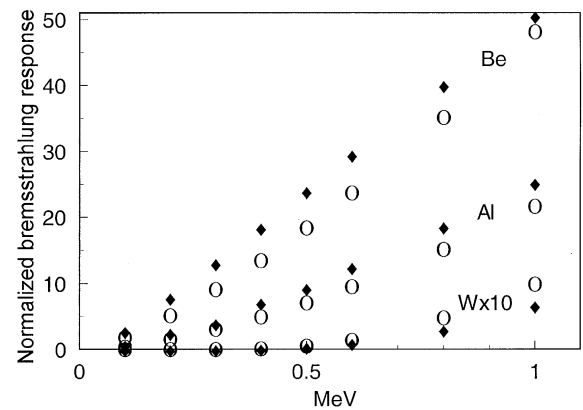


Fig. 7. Bremsstrahlung photon response, normalized to the geometrical response, for various incident electron energies. The normalized responses are calculated for the test case of Fig. 2(d) with beryllium, aluminum, and tungsten slab materials.



with  $E$  for the beryllium and aluminum cases. In general, an energy scaling  $\Gamma_b \sim E^{1-2}$  is obtained. The exponent depends on the thickness and  $Z$  value of the absorber and detector. The calculations in Fig. 7 show lower values of  $\Gamma_b/\Gamma_g$  for higher  $Z$  materials, which may seem somewhat counterintuitive. Although the photon production scales as  $Z^2$ , the exponential-like photon attenuation within the material dominates and results in smaller  $\Gamma_b/\Gamma_g$  ratios for larger  $Z$  values.

Supporting MC calculations of the bremsstrahlung yield are also performed for the slab geometry of Fig. 2(d). The number of source electrons is increased by a factor of four ( $N = 51.2$  million) for these calculations in order to obtain sufficient statistics. The ratios  $\Gamma_b/\Gamma_g$  obtained from the MC calculations are shown with open circles in Fig. 7 for the same cases as above. The two calculations are within 50% agreement for all cases in Fig. 7, in spite of some approximations for  $f_d$  for oblique cases.

Some of the MC counts are presumably caused by secondary electrons, although the distributions of deposited energy do not permit species identification. Secondary electrons are generated inside the slab as a result of photoelectric and Compton interactions. Only those secondary electrons generated within a distance  $R$  of the bottom of the slab can escape to deposit their energy into the detector. The photon differential flux  $dY/dk$  exiting the slab, given in Eq. (10), can be used to estimate the relative secondary electron contribution. This contribution is found negligible ( $<0.1\%$ ) for the beryllium and aluminum cases, but is of order 10% for most tungsten cases.

The relative contribution of secondary electrons to photons is approximately  $\mu R/\mu_d L_d$ , where  $\mu$  (slab) and  $\mu_d$  (detector) are evaluated at the mean photon energy. The numerator is the ratio of secondary electrons ( $\sim \mu R$ ) to photons ( $\sim 1$ ) that reach the detector. The denominator accounts for the different detection efficiencies ( $\sim 1$  for electrons,  $\sim \mu_d L_d$  for photons). The secondary electron contribution can be important when high  $Z$  materials, such as tungsten (high photoelectric  $\mu$ ), are used next to thin detectors (low  $L_d$  values). However, such contributions can be neglected here because the detector is very thick.

## 7. Satellite instrument example

We now apply the AP formalism to the BDD-IIR charged particle monitor. This instrument has been successfully launched on a Global Positioning Satellite (GPS) in November 2000. The BDD-IIR detectors measure the omnidirectional energetic particle fluxes impinging on the satellite 20,000 km above the Earth's surface [12]. We briefly describe below the solid-state instrument, the BDD-IIR box, and GPS satellite, since all contribute to the instrumental response.

### 7.1. The BDD-IIR instrument and the GPS satellite

The BDD-IIR energetic charged particle monitor consists of eight identical silicon detectors (disks of 8-mm diameter and 300- $\mu$ m thickness) located behind different absorbers [12]. We analyze here channel 3 of the BDD-IIR instrument. Its hemispherical beryllium, titanium, and gold absorber is sketched in Fig. 8(a). The beryllium includes five cylindrical gold collimators (1.5-mm diameter and 18.3-mm length) that yield a geometrical response  $\Gamma_g = 0.046 \text{ mm}^2 \text{ sr}$ . Beryllium filters (0.74-mm thickness) located at the bottom of the collimators define an electron energy lower threshold of about 0.48 MeV. The electronics discriminator counts all events for which an energy detector greater than 74 keV is deposited into the silicon detector.

The hemispherical absorber is mounted on top of an aluminum box ( $0.21 \times 0.11 \times 0.28 \text{ m}^3$  dimensions) sketched in Fig. 8(b). The thickness of the aluminum walls is 4.5 mm. The 35-mm high sensor deck below the dosimeters is essentially void, except for plastic detector mounts and electric wires. A piece of stainless steel (mass ballast of  $100 \times 100 \times 20 \text{ mm}^3$  dimensions) is located just below the sensor deck. The bottom portion of the box contains eight electronics modules.

The BDD-IIR box is mounted near a corner of the earth-facing top surface of the GPS satellite, as sketched in Fig. 9. The satellite outer surfaces define roughly a rectangular aluminum box ( $1.9 \times 1.5 \times 1.5 \text{ m}^3$  dimensions). Although the satellite walls have a complex honeycomb structure, they can be well approximated by an average

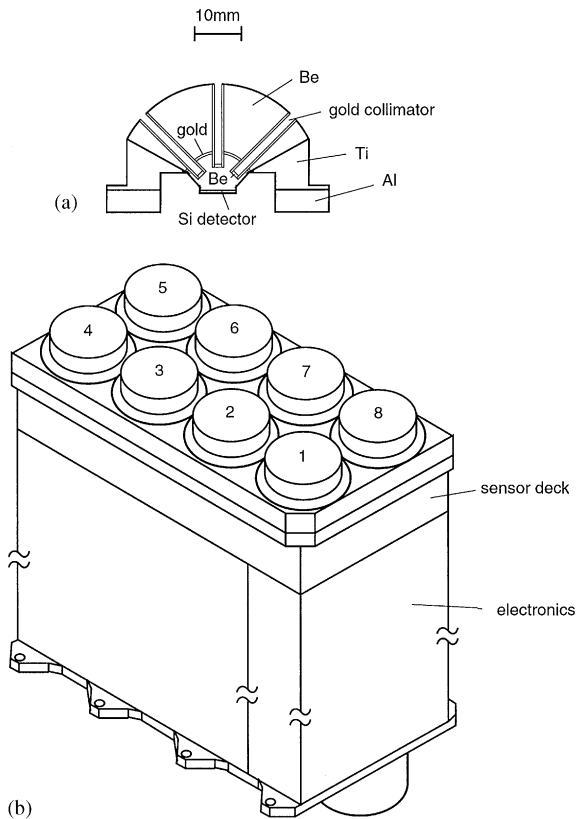


Fig. 8. Sketch of (a) the shield and detector of channel 3 of the BDD-IIR monitor, and (b) the flight box.

aluminum thickness of about 0.5 mm. Aluminum structural hardware, titanium propellant tanks, batteries, and electronics modules are found inside the satellite. The external antennas and solar panels shown in Fig. 9 are not important for this study because they are far away from the BDD-IIR box. However, the UHF and L-band antennas and the BDY optical sensor located on the top surface of the satellite must be considered in the calculations.

### 7.2. Calculated front responses

We calculate separately the contributions of the hemispherical absorber assembly, of the BDD-IIR box, and of the GPS satellite. The gathering power  $\Gamma$  of the absorber, calculated with the AP formalism and normalized to the geometrical response  $\Gamma_g = 0.046 \text{ mm}^2 \text{ sr}$ , is shown in Fig. 10

with solid diamonds for electron energies up to 7 MeV. Higher electron energies are not considered because there are too few such electrons at GPS satellite orbit. The open circles are the results of MC calculations with an isotropic, monoenergetic, hemispherical electron source around the absorber. The good agreement between the two calculations is somewhat fortuitous since the MC simulations use a slightly different geometry for the aluminum top plate.

The contributions of various processes to the AP front response are shown in Fig. 10 with solid curves labeled with a letter. The geometrical response (g) is essentially unity for all energies greater than the 0.48 MeV filter threshold of the gold collimators. There is a smooth increase between 0.48 and 1 MeV due to electron penetration of the filters. Collimator backscattering (s) is similar in shape as the geometrical response, and about half as large. Backscattering is substantial for high Z gold collimators. However, gold is hard to penetrate, so that the edge cut contribution (e) is negligible for most electron energies. There is no obvious choice for the collimator material because backscattering and edge cut contributions tend to compensate each other.

The bremsstrahlung contribution (b) from the beryllium, titanium, gold, and aluminum absorber is also indicated in Fig. 10. The ratio  $\Gamma_b/\Gamma_g$  scales approximately as  $E^2$  and clearly dominates the instrumental response between 2.5 and 5.5 MeV. A substantial number of photons generated in the absorber reach the silicon detector where they can deposit more than the 74 keV threshold energy through photoelectric and Compton interactions. Finally, primary electron penetration (p) of the large-area hemispherical beryllium absorber dominates for  $E > 6 \text{ MeV}$  but is negligible for  $E < 5 \text{ MeV}$ . Electron penetration is calculated in a way similar as for the edge cut in Section 5.

The responses in Fig. 10 can be used in Eq. (3) to derive instrumental count rates. The equatorial omnidirectional electron fluxes  $j_0$  in the earth's radiation belts can be approximated by two relativistic Maxwellian energy distributions [13]. There is a cold component of density  $n_1$  and temperature  $T_1$ , and a hot component of density  $n_2$  and temperature  $T_2$ . The average electron fluxes at

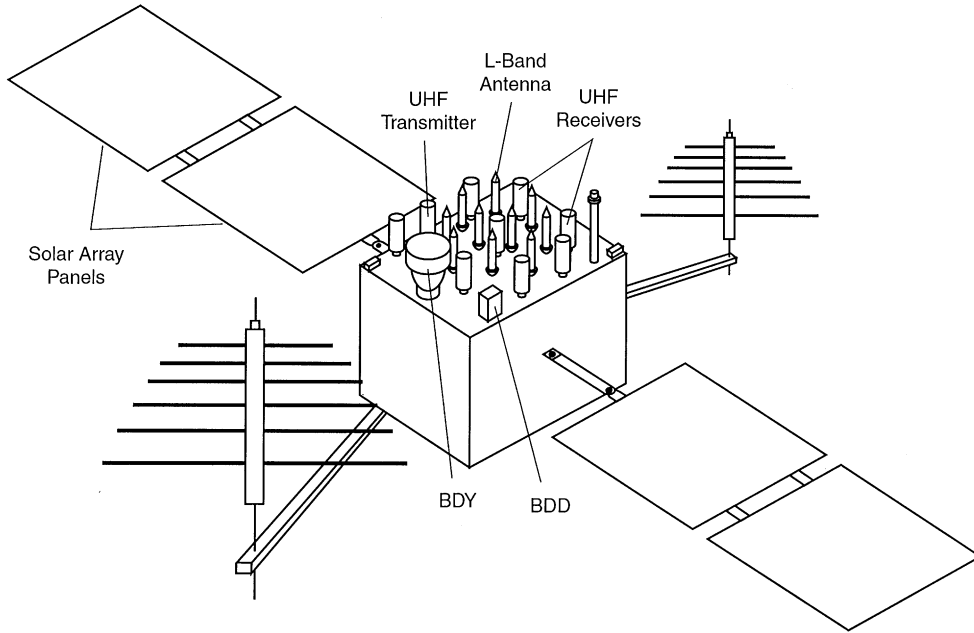


Fig. 9. Sketch of the GPS Block IIR satellite.

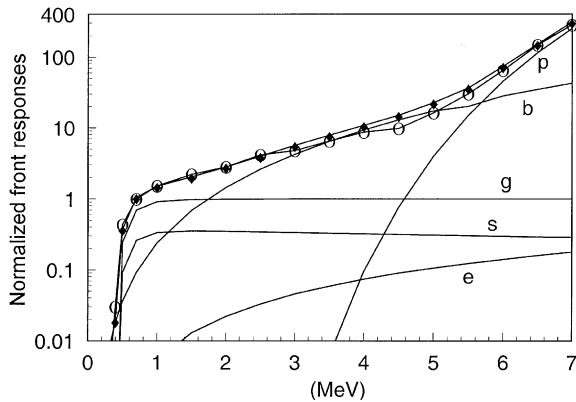


Fig. 10. Calculated front responses of channel 3 of the BDD-IIR charged particle monitor, normalized to the geometrical response, as functions of incident electron energy. The total front responses from Monte-Carlo and AP calculations are indicated with open circles and solid diamonds, respectively. The contributions of various processes to the AP total front response are indicated with solid lines labeled with a letter.

GPS orbit correspond to  $n_1 = 3000 \text{ m}^{-3}$ ,  $T_1 = 60 \text{ keV}$ ,  $n_2 = 600 \text{ m}^{-3}$ , and  $T_2 = 320 \text{ keV}$ . This average  $j_0$  yields 517 total front counts per second in the BDD-IIR-3 electron channel.

The total includes 283 geometrical counts, 3 edge cut counts, 86 wall scattering counts, and 144 bremsstrahlung counts.

Occasionally, during magnetic storm times, the hot electron population can be much larger. For example, one measured  $n_2 = 3000 \text{ m}^{-3}$  and  $T_2 = 450 \text{ keV}$  on March 24, 1991. For this case, one calculates 4723 front counts per second in the BDD-IIR-3 instrument, including 2006 from the geometry and 1985 from bremsstrahlung. Hence, the geometrical response is only 40–60% of the total front response for the above cases.

### 7.3. Calculated back responses

The satellite surfaces are continuously exposed to charged particles. In particular, energetic electrons create a significant bremsstrahlung photon flux in all directions. Some of these photons reach the back side of the detector and contribute to the instrumental response. Although such effects are too complex to be quantified with MC calculations, the AP formalism can be used to estimate them. We calculate separately the con-

tributions of the BDD-IIR box and of the rest of the satellite.

Cartesian coordinates, centered in the middle of the silicon detector, are used to define small rectangular surface elements. For any point  $P$  at the center of a surface element, we calculate the bremsstrahlung photon production and attenuation along a path  $PO$  with the formalism described in Section 6. The photon attenuations ( $\text{g}/\text{mm}^2$ ) are defined for the principal materials encountered (beryllium, carbon, aluminum, titanium, iron, and gold) as function of the polar angle  $\beta$  between  $PO$  and the vertical  $z$ -axis.

The calculated normalized responses of the box and satellite are shown with symbols in Fig. 11 as function of electron energy. The total (front + box + satellite) normalized response is also indicated with a solid curve in Fig. 11. The box and satellite contributions have similar ( $\sim E^2$ ) energy dependences. Surprisingly, the contribution of the  $0.2\text{ m}^2$  box is about a factor 2 higher than that of the  $20\text{ m}^2$  satellite surfaces. This occurs because surfaces closest to the detector dominate the bremsstrahlung yield. The detector solid angle,  $\Omega_d = A_d \cos(\beta)/PO^2$ , brings into Eq. (12) an inverse square distance weighting to the various surface elements. The  $\cos(\beta)$  of  $\Omega_d$  is cancelled in Eq. (13) by the thin detector absorption factor  $\sim \mu_d L_d / \cos(\beta)$ .

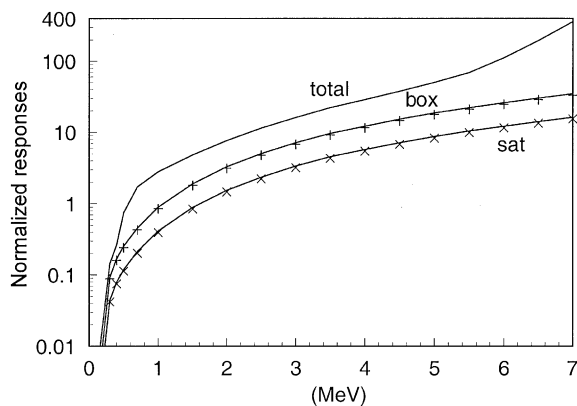


Fig. 11. Calculated AP contributions of the flight box and of the GPS satellite to channel 3 of the BDD-IIR monitor as functions of incident electron energy. The total response of the channel is also indicated. All responses are normalized to the geometrical response.

The importance of nearby surfaces is a recurring theme in these back response AP calculations. For example, the top surface of the box (excluding the channel 3 absorber) is the largest contribution to the box response. The top 25% of the vertical sides of the box contribute more than the bottom 75% of the vertical sides. The top surface of the satellite where the box is mounted contributes as much as all the other satellite surfaces. The UHF antennas (12%), L-band antennas (5%), and BDY sensor (3%) contribute about 20% to the overall back response. This percentage roughly reflects the respective external surface areas:  $4\text{ m}^2$  for the antennas and  $16\text{ m}^2$  for the satellite faces. Again, items closest to the BDD-IIR box are more important.

The back response AP calculations include many details of relatively minor importance. For example, the box contribution includes the additional electron flux that backscatters from the top satellite surface. This addition is somewhat offset by shadowing of the satellite surface by the box, an effect which is important on the surface elements close to the box. While the satellite bremsstrahlung photons come mostly from the thin aluminum skin of the satellite outer surfaces, there is some contribution from inner structures for high electron energies.

The back responses of Fig. 11 can be used in Eq. (3) to estimate the total instrumental count rates for the same  $j_0$  as for the front response. For the average  $j_0$  at GPS orbit, the BDD-II-R box and the rest of the satellite add 438 and 207 counts per second, respectively, to the 517 front counts previously calculated. For the storm time  $j_0$ , the box and the satellite add 4386 and 2070 counts, respectively, to the 4723 front counts. These examples indicate that the geometrical response of the collimators amounts to only about 20% of the total instrumental electron response, when the satellite structures are taken into account.

## 8. Discussion and conclusions

We have developed a new (AP) numerical technique, based on APs, that is, suitable to design and to evaluate the response of satellite charged

particle detectors. While the geometrical response is generally sufficient to characterize ion channels, this is not the case for energetic electrons. Angular scattering, material penetration, and bremsstrahlung radiation generally contribute substantially to the overall instrumental response. The AP formalism, summarized by Eqs. (1)–(3), requires an analytical expression for the detection efficiency and the computation of up to 5 integrals for each class of particle trajectory. A typical AP calculation, with a PC software such as Mathcad, takes less than 1 min of real time.

We have demonstrated the reasonable accuracy of the AP calculations by comparisons with MC simulations for a simple test case. Some approximations are necessary to define the analytical detection efficiencies. For example, the angular distribution of bremsstrahlung photon depends on local electron energy, an effect that must be averaged before convolution with incident electron directions and angular scattering. The AP formalism considers only the main classes of particle trajectories. Some higher order processes, such as multiple wall backscattering or combinations of edge cut, scattering, and photon production, are neglected. A complete AP calculation is probably accurate within about 50%, a reasonable balance between computational complexity and accuracy.

The usefulness of the AP calculation is perhaps best illustrated in Section 7, where the complex instrumental box and satellite contributions have been estimated for one electron channel of the BDD-IIR instrument. These contributions increase the instrumental response by a factor of 2–3, depending on the electron population at GPS satellite orbit. The AP calculations in Section 7 are perhaps the first quantitative estimates of box and satellite contributions to a charged particle instrument, although dose calculations for space microelectronics [14] also consider satellite structures. Some dose calculations are made with a discrete ordinates numerical technique that is faster but may require more computer memory than an MC simulation [15]. Dose calculations stress the importance of bremsstrahlung photons, and of photoelectrons issued from high  $Z$  surfaces near thin silicon electronics, in a way similar as in Section 6 of the present paper.

The AP formalism can be applied to more complex cases than the simple test case in this paper. We list here some examples that have been implemented, but have not been included in this paper. The geometrical response of Section 3 can easily be generalized to cases without azimuthal symmetry. The geometrical efficiency  $\varepsilon_g$  in Eq. (5) becomes the product of 4 Heaviside functions for rectangular collimators. If a three-element telescope is considered, additional Heaviside functions are included for the third aperture. The AP calculations of geometrical responses can also be extended to account for thin foil scattering. Each bottom aperture point  $Q$  becomes a circular area proportional to the scattering angle. The portion of the circular area that lies within the bottom aperture now defines the detection efficiency. Thin foil scattering of low-energy electrons can confuse the angular resolution of satellite instruments that use arrays of solid-state detectors behind an aperture lined with a light shield. The bremsstrahlung photon AP formalism, described in Section 6, can be applied to the response of X-ray sensors. Some combinations of photon source, filter, and silicon detector have already been considered.

The present AP calculations are sufficient to estimate all important instrumental effects in most cases. Future AP calculations could consider explicitly the energy distribution of the detected species. Energy resolution would be useful to evaluate the response of instruments that include differential rather than integral energy channels, and for comparisons of AP calculations with MC count distributions or with energy analyzer spectra. Last but not least, we found the AP calculations to be excellent teaching tools, since they yield much insight in the relative contributions and in the scaling laws of various processes.

### Acknowledgements

The authors wish to thank Stan Roeske from Sandia National Laboratory for kindly providing detailed information concerning the GPS Block IIR satellite. This work was performed under the auspices of the US Department of Energy.

## References

- [1] A.L. Vampola, Measurements techniques in space plasmas: particles, Geophysical Monograph 102, American Geophysical Union, 1998, p. 339.
- [2] J.D. Sullivan, Nucl. Instr. and Meth. 95 (1971) 5.
- [3] G.F. Knoll, Radiation Detection and Measurement, Wiley, New York, 1999.(Chapter 1)
- [4] J.F. Briesmeister, MCNP—a general Monte-Carlo N-particle code, Los Alamos National Laboratory Report LA-7396-M, 1986.
- [5] K. Siegbahn, Alpha-, Beta-, and Gamma-Ray Spectroscopy, Vol. 1, North-Holland Publishing Company, Amsterdam, 1965.
- [6] G. Moliere, Z. Naturforsch. 3a (1948) 78.
- [7] Von H. Frank, Z. Naturforsch. 11a (1959) 247.
- [8] T. Tabata, R. Ito, S. Okabe, Nucl. Instr. and Meth. 94 (1971) 509.
- [9] R.D. Evans, The Atomic Nucleus, McGraw-Hill Book Company, New York, 1955.(Chapter 21)
- [10] J. Marshall, A.G. Ward, Can. J. Res. A 15 (1937) 39.
- [11] H. Ferdinande, G. Knuyt, R. Van De Vijver, R. Jacobs, Nucl. Instr. and Meth. 91 (1971) 135.
- [12] T.E. Cayton, D.M. Drake, K.M. Spencer, M. Herrin, T.J. Wehner, R.C. Reedy, Description of the BDD-IIR: electron and proton sensors on the GPS, Los Alamos Report LA-UR-98-1162, 1998.
- [13] T.E. Cayton, R.D. Belian, S.P. Gary, T.A. Fritz, D.N. Baker, Geophys. Res. Lett. 16 (1989) 147.
- [14] W.C. Fang, C.R. Drumm, S.B. Roeske, G.J. Scrivner, IEEE Trans. Nucl. Sci. NS43 (1996) 2790.
- [15] L.J. Lorence, IEEE Trans. Nucl. Sci. NS39 (1992) 1031.